Jacob, D. E., Wirth, R., Soldati, A. L., Wehrmeister, U., Schreiber, A. (2011): Amorphous calcium carbonate in the shells of adult Unionoida. - Journal of Structural Biology, 173, 2, 241-249

DOI: 10.1016/j.jsb.2010.09.011

Amorphous calcium carbonate in the shells of adult *Unionoida*

D.E. Jacob[1*], R. Wirth[2], A. L. Soldati[1+], U. Wehrmeister[1], A. Schreiber[2]

1 Earth System Science Research Centre and Department of Geosciences, Johannes Gutenberg Universität, J.J. Becherweg 21, D-55099 Mainz, Germany

2 GeoForschungsZentrum Potsdam, Telegrafenberg C120, D-14473 Potsdam, Germany

[+] now at: CONICET, Centro Atómico Bariloche, Av. Bustillo 10500, CP8400 San Carlos de Bariloche, Argentina

* corresponding author: jacobd@uni-mainz.de

Abstract

Shells of adult individuals from two different bivalve families, *Hyriopsis cumingii* and *Diplodon chilensis patagonicus*, were studied by Micro Raman spectroscopy and Focussed Ion Beam-assisted TEM. The shells contain amorphous calcium carbonate in a zone at the interface between the periostracum and the prismatic layer. In this area, the initial prism structures protrude from the inner periostracum layer and it is demonstrated that these structures systematically consist of highly disordered and amorphous calcium carbonate. Within this zone, ordered and disordered areas are intermingled discounting the existence of a crystallization front and favouring models of domainal crystallization processes via so-called mesocrystals. These observations are the first documentation of the use of amorphous calcium carbonate as a precursor phase by adult mollusc species and lend further support to hypotheses postulating widespread use of amorphous phases as building material of skeletal tissue in biology.

Keywords: Amorphous calcium carbonate, *Hyriopsis cumingii, Diplodon chilensis patagonicus*, Raman spectroscopy, FIB-TEM, vaterite

1. Introduction

1.1 The nanostructure of bivalve shells

The mechanisms of bivalve shell growth have fascinated and inspired generations of researchers. Intensive research across disciplines unveiled a complex picture of a highly organised structure involving both organic and inorganic components. However, the majority of the exact metabolic pathways as well as the molecular mechanisms which lead to the development of this bio-engineered material are still enigmatic.

Major advances are tightly coupled to the development of high resolution instrumental analytical methods like, for example, Transmission Electron or Atomic Force Microscopy that allow observation at the nanometre scale. Studies using such nano-scale methods showed that nacre platelets and prisms are not single crystals (Mutvei, 1977), but consist of highly aligned crystals of aragonite or calcite at the nanometre scale (Metzler et al., 2007) which have been termed mesocrystals (Niederberger and Cölfen, 2006). The basic building units of these and all higher structures in bivalve shells are minute $CaCO_3$ vesicles in the order of ca. 20-50 nanometres (e.g. Addadi et al, 2006, Dauphin, 2008, Jacob et al., 2008). Element mapping using electron energy-loss spectrometry by TEM provided direct evidence for an organic membrane coating each individual $CaCO_3$ vesicle (Jacob et al., 2008). These organic membranes permanently coat the $CaCO_3$ and are incorporated in the crystal lattice of aragonite and calcite upon assemblage of the much larger tablet and prism structures. This leads to characteristic distortions of the aragonite or calcite crystal lattice that can be traced by X-ray diffraction (Pokroy et al., 2006).

Descriptions of such $CaCO_3$-bearing vesicles in cells close to the mineralization site can be found throughout the literature (e.g. Cartwright and Checa, 2007; Neff, 1972; Watabe et al., 1976) and imply active cellular transport of $CaCO_3$ to the site of mineralization, for example by haemocytes (Mount et al., 2004), rather than precipitation from oversaturated solutions.

1.2 Amorphous Calcium Carbonate in mollusc shells

Jacob et al. (2008) showed for freshwater cultured pearls from *Hyriopsis* sp. that $CaCO_3$ contained in these vesicles is initially an amorphous phase which subsequently crystallizes to form aragonite. Amorphous calcium carbonate (ACC) is frequently discussed to be the precursor phase in biology in general (Weiner, 2008) and in mollusc shell formation processes in particular: larval shells of the marine bivalves *Mercenaria mercenaria* (Linnaeus, 1758) and *Crassostrea gigas* (Thunberg, 1793) for example, were found to form entirely from amorphous calcium carbonate that subsequently transformed into the crystalline mineral phase (Weiss et al., 2002). Similarly, larval shells of the freshwater gastropod *Biomphalaria glabrata* (Preston, 1910) initially consist completely of ACC (Hasse et al., 2000). The finding of ACC in larval shells of such diverse species of molluscs led to the

hypothesis that the use of amorphous $CaCO_3$ as the precursor of the crystalline phase may be a basic strategy (Addadi et al., 2003; Weiss et al., 2002). However, up to now findings of ACC as a constituent phase in shells were restricted to the larval stage, while there is only one report of ACC in an adult mollusc shell (Nassif et al., 2005). These authors found an ACC coating around a nacre tablet in the shell of *Haliotis laevigata* and interpreted this amorphous coating to be stabilized by impurities which were expelled from the amorphous precursor phase upon crystallization into aragonite.

ACC in freshwater cultured pearls from *Hyriopsis cumingii* x *Hyriopsis schlegelii* hybrids are found close to the innermost organic layer in the pearls (Jacob et al. 2008). Pearl culturing makes use of the identical natural processes to those that form the mussel shell, and pearls can therefore be used as structural analogues to shells, although showing a distinctly inverted geometry. The zone containing ACC in the pearls is the area in which pearl mineralization starts and corresponds structurally to the interface between the inner periostracum and the prismatic layer in bivalve shells. Consequently, we report here on the systematic occurrence of amorphous calcium carbonate in this interface zone in shells in two different *Unionoid* species and argue that ACC could be the regular building material, supporting the hypothesis that it is possibly widespread in the phylum.

2. Materials and Methods

2.1 Bivalve samples

Valves of two different mussel species, *Hyriopsis cumingii* (Lea, 1852) and *Diplodon chilensis patagonicus* (d'Orbigny, 1835) were studied. The bivalves are of the order of *Unionoida* (Stoliczka, 1871) and belong to the *Unionidae* and *Hyriidae* families, respectively. Valves of *Hyriopsis schlegelii* and *Diplodon chilensis patagonicus* are equivalve, covered with a thick periostracum and consist exclusively of aragonite. The genus *Hyriopsis* is native to East Asia. *Hyriopsis cumingii* (Lea, 1852) and *Hyriopsis schlegelii* (Martens, 1861) are the two main pearl-producing species native to Japan and China, respectively (Graf and Cummings, 2007). A non-specified hybrid of these two species is increasingly used for pearl culturing in Japan as this yields better harvests (Fiske and Shepherd, 2007). Valves can be as large as 25 cm and individuals can live as long as 40 years (Strack, 2006); the sample of *Hyriopsis cumingii* used here was collected alive from a pearl farm in Wuhan, China in 2007 and was six years old at the time of collection.

Bivalves of the genus *Diplodon* are geographically widely distributed and occur in most areas of the southern hemisphere. The subspecies *Diplodon chilensis patagonicus* is native to Patagonia and populations are reported in Argentina between Mendoza (32° 52' S; 68° 51' W) and Chubut (45° 51' S; 67° 28' W; Castellanos, 1959). Samples used in this study were collected alive in 2007 from the lakes of the Nahuel Huapi National Park in Patagonia,

Argentina (41°S; 71°W). Individuals are long-lived (90 years and more; Soldati et al., 2009) and valves reach sizes of ca. 12 cm. The age of the shell used in this study was determined as at least 26 years by counting the internal growth rings after cutting the shell dorsal-ventral along the axis of maximum growth and staining with *Alcian Blue* to highlight the annual growth lines (for a detailed description see Soldati et al., 2009).

The shells were cut and mounted in epoxy resin (Struers, Willich, Germany), then polished using 800 and 1200 Al_2O_3 powder followed by a last polishing step with 1µm Al_2O_3 powder on a Buehler G-cloth. Light microscopy investigations were carried out with a VHX-600 digital microscope (KEYENCE, Neu-Isenburg; Germany), equipped with a VH-Z25 zoom lens (magnification from 25x to 175x) or a VH-Z50 long-distance, high-performance zoom lens with a magnification of up to 5000x.

2.2 Raman spectroscopy and XRD

Raman spectra were recorded at room temperature using a Horiba Jobin Yvon LabRAM HR spectrometer equipped with a Si-based CCD-detector (Peltier-cooled) and an integrated Olympus BX41 optical microscope (100x magnification) with automated stage. The 532.2 nm line of a Nd-YAG laser line was used for excitation with a laser power of 90 mW. The Rayleigh radiation of the laser was blocked using edge filters and the scattered light was dispersed by a grating with 1800 grooves/mm. Data acquisition and spectra treatment was carried out with the commercially available program LabSpec v4.02 (Horiba Jobin Yvon). Due to the sensitive nature of amorphous calcium carbonate, Raman spectra were recorded once and with short acquisition times (2s per window). Laser spot size was 2µm. Peak analysis was performed with Origin-lab® 7.5 Pro by fitting the peaks as either single or overlapping Lorentzian and Gaussian curves.

2.3 Focused Ion Beam-assisted Transmission Electron Microscopy

For Transmission Electron Microscope analyses (TEM) at the GeoForschungsZentum Potsdam, ultra-thin foils of ca. 10 by 15 µm and 0.150 – 0.200 µm thicknesses were prepared using the focussed ion beam device (FIB) of a FEI FIB200 instrument following procedures given in Wirth (2004). After milling, the foil was cut free, lifted out, and placed on a carbon coated Cu grid. No further carbon coating was necessary. The FIB-milling method is carried out by sputtering the material surrounding the target area with gallium ions. The target area itself is protected by a platinum coating. Heating of the sample during sputtering has been shown to be less than 10 K, due to the very low angle between Ga beam and sample (Ishitani and Yaguchi, 1996). However, it is well known that FIB-milling generates a thin amorphous layer of 10- 20 nm thickness on both sides of the foil and that its thickness shows a strict linear relationship to the accelerating voltage of the Ga beam (e.g. Kato 2004). The

thickness of this layer is much less than the total thickness of the foil (150-200 nm) and causes nothing more than a slight blurring effect in high resolution TEM images, if not removed. Amorphisation introduced by FIB milling across the complete thickness (or considerable parts) of the foil has never been observed, an observation which is supported based on the experience with producing and examining more than 2000 FIB foils in this laboratory. We consider it therefore highly unlikely that the amorphous phases studied here are introduced by the FIB-milling procedure.

TEM imaging and analysis were undertaken with a FEI Tecnai™G2 F20 X-Twin transmission electron microscope with a field emission gun electron source. The TEM was operated at 200 kV acceleration voltage. A Gatan Tridiem™ filter allowed energy-filtered imaging applying a 20 eV window to the zero loss peak. The Gatan system was also used for electron energy-loss spectroscopy (EELS). Analytical electron microscopy (AEM) was performed with an energy dispersive X-Ray analyzer (EDX). Analyses were usually carried out in scanning transmission mode (STEM) scanning the beam in a pre-selected window thus avoiding mass loss during the spectrum acquisition. Counting time was 60 -120 seconds. Beam size was approximately 1 nm in diameter.

Great care was taken to minimize radiation damage to the material during analysis. At the start of the analyses, an overview picture was taken and the sample was examined critically at low magnification under a defocused beam. In this way, crystalline and amorphous areas were recorded and episodically repeated careful visual examination during the analytical session confirmed the unchanged nature of the sample. Furthermore, all analyses requiring a focused electron beam and high resolution TEM (HRTEM) were carried out at the very end of the analytical session. Nevertheless, the last of these HRTEM analyses is suspected to have created radiation damage to the sample which is described in detail in the discussion section.

3. Results

3.1 Light microscopy: Shell structure

All shells studied here consist entirely of aragonite and display a so-called “simple prismatic structure” (Carter, 1980), consisting of a dorsal prismatic layer followed by a nacreous layer towards the inside (Fig. 1a). Prism and nacre layer have different thicknesses in the different specimens with the largest (*Hyriopsis cumingii*) showing the thickest nacre layer (5-8 mm) and a relatively thin prismatic layer of ca. 200 µm, while the much smaller *Diplodon chilensis patagonicus* has a ca. 1000 µm thick prismatic layer and a nacre layer of 2-4 mm thickness. Single prisms are typically 40 by 200 µm in *Hyriopsis* and ca. 10 by 300 µm in *Diplodon chilensis patagonicus*.

Although all shell structures in molluscs are a combination of inorganic and organic material at the nanometre-scale (e.g. Lowenstam and Weiner, 1989), the prism structures contain

considerably less chitin than the nacre layer (Nudelman et al., 2007). The periostracum, which has been shown to play a major role in the growth of the prism layer (Checa, 2000; Petit et al., 1980a, b), is a two-layered structure in unionid bivalves, formed by the mantle epithelium and covering the mineral part of the shell towards the outside (Bevelander and Nakahara, 1967; Checa, 2000). Initial $CaCO_3$ prisms protrude from within the inner periostracum as spherulitic, rounded structures (e.g. Checa, 2000; Ubukata, 1994), before the prismatic morphology develops. Not all "prism seeds", however, develop into even prisms (Fig. 1b, c). Depending on the growth rate of the shell and geometric factors, such as the angle between individual prism and periostracum and curvature of the shell, competition for space and geometrical selection leads to growth of some prisms at the expense of others (Ubukata, 1994). Examined under reflected light, initial prisms protruding from the inner periostracum in all shells appear darker (i.e. have lower reflectance) than those further towards the ventral side of the shell (Fig. 1c).

A section of the shell in a dorsal-ventral direction along the axis of maximum growth reveals that periostracum and prism layers are duplicated in some areas of the shell (Fig. 1a, arrows). Overlapping prism layers are divided by growth lines that extend from the prismatic into the nacreous layer and can be accompanied by extension of the periostracum into the nacre layer (Checa, 2000). These dark organic layers have been described as "annual bands" or "pseudoannuli" (Coker et al., 1921) or as "intra-shell periostracum" (Checa, 2000) and are caused by prolonged interruption and subsequent resumption of shell growth. In adult *Diplodon chilensis patagonicus* as well as in many other bivalve species (e.g. *Margaritifera margaritifera, Arctica islandica, etc.)*, major growth lines, with or without intra-shell periostracum, have been found to occur regularly once a year and are caused by reduction of growth during the reproduction period of the individuals (e.g. Schöne et al., 2004; Soldati et al., 2009). Additional finer growth lines (Fig. 1c, arrow) delineate subannual shell growth increments (e.g. Barker, 1964; Clark II, 1974) and cause the characteristic horizontal "striping" of the prisms frequently observed during SEM imaging (e.g. Checa, 2000; Ubukata, 1994). The fact that these growth lines traverse prisms and nacre platelets alike attests to the simultaneous formation of prism and nacre layer during shell growth.

3.2 *Micro-Raman Spectroscopy*

Figure 2 compares the typical Raman spectrum of crystalline biogenic aragonite, represented by the nacre layer of *Diplodon chilensis patagonicus* (spectrum d), with spectra from the initial prisms at the interface with the periostracum of *Hyriopsis cumingii* (a) and *Diplodon chilensis patagonicus* (b). Plotted in Fig. 2a and b for further comparison is a spectrum of ACC from the sternal $CaCO_3$ deposits of a woodlouse (*Porcellio scaber, crustacea*) measured at identical conditions (spectrum c). Woodlice have been shown to form cuticular

231 deposits of stable amorphous calcium carbonate during moulting (Ziegler 1994, 1997). The
232 amorphous character of this phase has been confirmed and is well documented in several
233 studies (e.g. Becker et al., 2003, Hild et al., 2008, Tao et al., 2009).
234 Compared to crystalline aragonite from the shell nacre layer, the Raman spectra of the initial
235 prisms show a much lower intensity for all aragonite Raman bands. Furthermore, the main
236 Raman band of the carbonate ion (ν_1 at 1085cm^{-1}, White, 1974) is shifted towards lower
237 wavenumbers and is broader (i.e. shows a higher value for the full width at half maximum;
238 FWHM) than for well crystallized aragonite (Fig. 2b). Lastly, the bands in the 100-300cm^{-1}
239 region of the Raman spectra of crystalline aragonite, which are caused by vibrations of the
240 aragonite crystal lattice (White, 1974), are not detectable in the three prism spectra. These
241 features are typical for highly disordered (i.e. amorphous) materials and agree closely with
242 the features of the ACC spectrum of *Porcellio scaber* (Fig. 2a, spectrum c).
243
244 *3.3 TEM analyses*
245 To study the ACC areas at higher resolution, a section of a *Hyriopsis cumingii* shell was
246 chosen exemplarily for FIB-assisted TEM analysis. Figure 1d shows the pit in the shell
247 section left by Focused Ion Beam (FIB) milling. The FIB-foil (Fig. 3a) straddles the
248 periostracum-prismatic layer interface and was cut free from the positions marked with "X".
249 These marks are used during FIB-milling for re-alignment following instrumental drift. TEM
250 analyses concentrated on an area in one of the initial prisms adjacent to the periostracum,
251 marked with a white square in Fig. 3a. The calcium carbonate in the prism shows the typical
252 vesicular nanostructure (Fig. 3b-f) common to many mollusc species (Addadi et al., 2006;
253 Dauphin, 2008, Jacob et al., 2008) as well as to sea urchins (Beniash et al., 1997). Several
254 authors have shown that the vesicles in bivalves are contained in individual organic sheaths
255 (Dauphin et al., 2008, Jacob et al., 2008) and are held together by an organic mesh (Jacob
256 et al., 2008), some of whose fibres can be seen in Fig. 3c (arrows).
257 TEM dark field imaging reveals that the vesicles represent a mixture of amorphous areas
258 without diffraction contrast (Fig. 3d, arrows) and crystallized domains in which crystallites
259 show up as white spots as small as 5-10 nm in Fig. 3d. It is important to note that the
260 material showing these differences in crystallinity consists mainly of calcium carbonate as
261 shown by EELS mapping, with high calcium (Fig. 3e) and low carbon concentrations (Fig. 3f)
262 and that organic material is only present in minor amounts.
263 One vesicle (Fig. 3c, d, black frame) with very few crystallites was used for HRTEM analysis.
264 The vesicle was analysed along a profile from rim to core in three areas of ca. 35 nm in size
265 (Fig. 4a, white line). The HRTEM image of the vesicle rim (Fig. 4b) shows that this area is
266 almost entirely free of crystalline areas, marked by a nearly complete lack of lattice fringes.
267 Only a very small area of ca. 5 nm was found to show lattice fringes (circled area). These

findings, i.e. dominant amorphous areas with minor crystallized domains, apply also to other areas towards the centre of the vesicle (Fig. 4c, d). The area in the centre of the vesicle which was analysed last, however, shows the highest amount of crystalline nanodomains. These are arranged in an intimate mixture of crystalline and amorphous areas in which the crystalline domains appear to be randomly oriented as shown by their lattice fringes (Fig. 4d). Lattice-spacing (d-spacing) values for all three areas, calculated from the respective FFT (Fast Fourier Transform) analyses (Figs. 4f, g) are tabulated in Table 1. Most values are consistent with literature values for aragonite as well as with those for vaterite. However, one characteristic value of 3.16 Å for the d-spacing in the centre of the vesicle is clearly indicative of calcite.

4. Discussion

Micro-Raman spectroscopy identified ACC at the periostracum-prismatic layer interface in the shells of both studied species. This structural context is in accordance with what was to be expected from our studies on pearls, where ACC was identified at the interface between the innermost organic lamella and the prismatic layer (Jacob et al., 2008). These structures are the pearl analogues to periostracum and prismatic layer in the shells, and support the view that pearls can be studied as pathological, but nevertheless structural analogues to shells.

A closer look with TEM shows that the crystallinity of $CaCO_3$ in this interface area is variable: amorphous areas are intermingled with nano- and micro-domains of crystalline material (Fig. 3d). The vesicle chosen for HRTEM profiling (Fig. 4a) consists mainly of ACC with subordinate crystalline nano-domains. This strongly suggests that ACC is the original carbonate phase and precursor to the crystallized polymorph. It should be noted, however, that compared to the dark field TEM overview image (Fig. 3d), the high resolution images show more crystalline areas in the centre of the vesicle (Fig. 4d). As the high resolution analysis at this spot was carried out last, we think it likely that crystallization here was induced by the electron beam and that the centre of the vesicle originally contained more disordered $CaCO_3$, similar to the rim. Calcite detected in the centre of the vesicle (Table 1) is taken as further evidence for radiation damage, as the occurrence of this phase is restricted to the centre spot which was longest exposed to the electron beam and otherwise has never been reported in *Hyriopsis cumingii* shells.

A number of studies reported vaterite in biominerals (e.g. Hasse et al., 2000, Soldati et al., 2008, Lowenstam and Weiner 1989), and some have argued that this mineral is a regular intermediate phase in the biomineralization pathway to aragonite or calcite (e.g. Gago-Duport et al., 2008; Hasse et al., 2000). However, in contrast to this study, most of these

occurrences are apparent repair structures which do not represent regular shell growth pathways. Therefore, growth structures here were carefully analysed for the possible occurrence of vaterite.

At the resolution of Micro-Raman spectroscopy of ca. 2µm, vaterite was never encountered along the ca. 20 µm wide ACC-bearing zone at the periostracum interface of either of the two bivalve species studied. This precludes a major role of vaterite during aragonite crystallization from ACC. At nanometre resolution, the occurrence of vaterite can neither be confirmed nor ruled out from the HRTEM analyses. All d-spacing values (except for one indicative of calcite) can be assigned to lattice planes of aragonite as well as to vaterite, if measurement uncertainties for FFT analyses of ca. 0.01 nm are taken into account (Table 1). It should be noted that generally only few reflections differentiate vaterite clearly from aragonite and not all reflections are observed in every measurement. In our case, it is mainly the vaterite (100) = 0.357 nm reflection, as opposed to the aragonite (111) = 0.397 nm reflection (Table 1). An observed d-spacing value of 0.346 nm for the centre of the vesicle (Fig. 4g and Table 1) could possibly indicate vaterite in a nano-domain. However, this evidence is weak, especially since this area is believed to have experienced some radiation damage.

Taking all evidence together, it appears that ACC is the precursor phase of aragonite in the shells and that biomineralization proceeds directly without evidence of vaterite as an intermediate product.

The TEM analyses (Fig. 3d) show that no coherent mineralisation front is developed, a finding that compares favourably with studies on sea urchin larval spicules. Using X-ray photoelectron emission spectromicroscopy, Politi et al. (2008) showed that amorphous calcium carbonate and the corresponding crystalline phase, in this case calcite, were juxtaposed on a scale of tens of nanometres. These authors speculated that crystallization emanated from nano-domains, 40-100 nm in size, which stimulated further crystallization in adjacent domains. This observation is supported for the nanostructure of nacre platelets in *Haliotis refuscens* (Li and Huang, 2009) that show nanocrystals in similar sizes connected by screw dislocations and unidentified amorphous material resulting in a pseudo-single crystal or mesocrystal (Cölfen and Antonietti, 2005). The alignment mechanisms of the nanocrystals, however, are not fully understood and possibilities comprise epitaxial crystallization via mineral bridges (Schäffer et al., 1997), Ostwald ripening processes (e.g. Gago-Duport et al., 2008) to alignment of freely crystallized nano-particles via short range physical forces, such as interface energies, capillary forces, etc. Although it is currently difficult to substantiate whether mineral bridges are the cause or the effect of mesocrystal formation, they are omnipresent at all scales, i.e. between nano-particles, between

membrane coated vesicles (Jacob et al., 2008) and between individual tablets in mollusc nacre (e.g. Li and Huang, 2009).

Sizes of the nano-domains are well below the 2 µm resolution of the Micro-Raman spectrometer. Raman spectra of ACC in this study, and probably in many other cases of biogenic ACC, are therefore mixtures of amorphous and crystalline fractions in variable amounts. The observed broadening of the v_1 band at ca. 1080 cm^{-1} is therefore not only caused by the disordered state of the material, but also results from addition of the v_1 band of the crystalline phase situated at slightly higher wavenumbers, resulting in an asymmetric shape of the v_1 band (Wehrmeister et al., in press).

The amino acid composition of the molluscan periostracum contains considerable amounts of aspartic and glutamic acid (Meenakshi et al., 1969) which are thought to be the main active bio-molecules in the stabilization of ACC (Aizenberg et al., 1996). Furthermore, Checa (2000) demonstrated that the inner periostracum in bivalves is produced by the same outer mantle epithelial cells that simultaneously secrete the prismatic and nacreous shell layers. It is therefore proposed here that ACC, as the originally building material of the shell, is preserved at the edge of the inner periostracum due to the high organic to mineral ratio in this zone, whereas it is rapidly transformed into the crystalline phase further away. In this light, it would be interesting to investigate possible chemical similarities of the inner periostracum, interprismatic layers and nacreous interlamellar sheets further to clarify its role in the biomineralization of mollusc shells.

6. Conclusions

Up to now, the occurrence of an amorphous phase in the shells of adult mollusc species was often suspected, but with little success in providing direct proof for its existence. While ACC has been observed in larval mollusc (Hasse et al., 2000; Weiss et al., 2002) and juvenile bivalve shells (Baronnet et al., 2008), only one study exists that reports the occurrence of amorphous calcium carbonate in the shell of an adult individual (Nassif et al., 2005). These authors discovered continuous amorphous coatings of ca. 3 to 5 nm size around each nacre platelet within shells of the gastropod *Haliotis leaevigata*. The structural context of these coatings, however, remained unclear and it was speculated that they resulted from a process similar to zone-refining that expelled impurities from the aragonite crystals which, in turn, kinetically stabilized the amorphous phase.

Here we demonstrate the occurrence of ACC in shells of two adult bivalves belonging to different families, while evidence for the involvement of vaterite is lacking. We show that the amorphous phase is not randomly distributed, but is systematically found in a narrow zone at

379 the interface between periostracum and prism layer. This zone is the area where spherulitic
380 $CaCO_3$-structures protrude from the inner periostracum to form the initial prisms (Checa,
381 2000). These observations are in accordance with our earlier results on equivalent structures
382 in freshwater cultured pearls (Jacob et al., 2008) and show that the original building material
383 for the prisms is amorphous calcium carbonate, secreted in vesicles at the inner
384 periostracum layer. As the nacre layer of many other mollusc species consists of membrane-
385 coated crystalline $CaCO_3$ vesicle, too (Addadi et al., 2003; Dauphin 2008; Jacob et al., 2008),
386 it is viable to suspect a much broader role for ACC as building material of biological hard
387 tissues.
388 The growing evidence for a common use of ACC as a transient precursor phase of crystalline
389 $CaCO_3$ by adult individuals from different bivalve families, even by different evolutionary
390 unrelated phyla such as molluscs and echinoderms is highly intriguing. It should be noted
391 that even within the mollusc phylum, the use of ACC as a precursor to crystalline $CaCO_3$
392 appears to have developed independently during evolution (Jackson et al., 2010).
393 These findings clearly underline the general importance of amorphous phases as plastic
394 building material in hard tissues (e.g. Addadi et al., 2003). However, the exact mechanisms
395 of biomineralization are still largely unknown and it will have to be the aim of studies of both
396 biomimetic and natural systems to shed light on this area.
397
398
399 **5. Acknowledgments**
400 We thank the Johannes Gutenberg University (Mainz) and the Earth System Science
401 Research Centre (Geocycles) for financial support. Crystallographic discussions with R.
402 Meffert and H.-D. Werner are greatly appreciated. Comments from two anonymous
403 reviewers are gratefully acknowledged.
404
405 **6. References**
406 Addadi, L., Raz, S. and Weiner, S., 2003. Taking advantage of disorder: Amorphous calcium
407 carbonate and its roles in biomineralization. Adv. Mater. 15: 959-969.
408 Addadi, L., Joester, D., Nudelman, F. and Weiner, S., 2006. Mollusk shell formation: A
409 source of new concepts for understanding biomineralization processes. Chem. Eur. J.
410 12: 980-987.
411 Aizenberg, J., G. Lambert, L. Addadi, and S. Weiner, 1996. Stabilization of amorphous
412 calcium carbonate by specialized macromolecules in biological and synthetic
413 precipitates. Advanced Materials 8: 222-226.
414 Barker, R.M., 1964. Microtextural variations in pelecypod shells. Malacologia 2: 69-86.
415 Baronnet, A., Cuif, J.P., Dauphin, Y., Farre, B. and Nouet, J., 2008. Crystallization of
416 biogenic Ca-carbonate within organo-mineral micro-domains. Structure of the calcite
417 prisms of the Pelecypod *Pinctada margaritifera* (Mollusca) at the submicron to
418 nanometre ranges. Mineralogical Magazine 72: 617-626.

Becker, A., Bismayer, U., Epple, M., Fabritius, H., Hasse, B., Shi, J. and Ziegler, A., 2003. Structural characterisation of x-ray amorphous calcium carbonate (ACC) in sternal deposits of the crustacea *Porcellio scaber*. Dalton Trans.: 551-555.

Beniash, E., Aizenberg, J., Addadi, L. and Weiner, S., 1997. Amorphous calcium carbonate transforms into calcite during sea urchin larval spicule growth. Proc R Soc London B 264: 461-465.

Bevelander, G., and H. Nakahara, 1967. An electron microscope study of the formation of the periostracum of Macrocallista maculata. Calc. Tiss. Res. 1: 55-67.

Carter, J.G., 1980. Environmental and biological controls of bivalve shell mineralogy and microstructure, in: D. C. Rhoads and R. A. Lutz (Eds.), Skeletal Growth of aquatic organisms, Plenum Publ. Corp., New York.

Cartwright, J.H.E., and Checa, A.G., 2007. The dynamics of nacre self-assembly. Journal of the Royal Society Interface 4: 491-504.

Castellanos, Z.A. 1959. Las especies del género Diplodon en la Argentina., pp. 85-94 1º Congreso Sudamericano Zoología, Vol. 2, La Plata, Argentina.

Checa, A.G., 2000. A new model for periostracum and shell formation in Unionidae (Bivalvia, Mollusca). Tissue Cell 32: 405-416.

Clark II, G.R., 1974. Growth lines in invertebrate skeletons. Annual Review of Earth and Planetary Sciences 2: 77.

Coker, R.E., Shira, A.F., Clark, H.W. and Howard, A.D., 1921. Natural history and propagation of freshwater mussels. Bull. Bur. Fish. 37: 75-181.

Cölfen, H., and Antonietti, M., 2005: Mesocrystals: Inorganic superstructures made by highly parallel crystallization and controlled alignment. Angew. Chemie Int. Ed., 44: 5576-5591.

Dauphin, Y., 2008. The nanostructural unity of Mollusc shells. Mineralogical Magazine 72: 243-246.

Fiske, D., and Shepherd, J., 2007. Continuity and change in Chinese freshwater pearl culture. Gems & Gemology 43: 138-145.

Gago-Duport, L., Briones, M.J.I., Rodríguez, J.B., and Covelo, B., 2008. Amorphous calcium carbonate biomineralization in the earthworm's calciferous gland: pathways to the formation of crystalline phases. J. Structural Biology 162: 422-435.

Graf, D.L., and K.S. Cummings, 2007. Review of the systematics and global diversity of freshwater mussel species (Bivalvia:Unionoida). J. Molluscan Studies 73: 291-314.

Hasse, B., Ehrenberg, H., Marxen, J.C., Becker, W. and Epple, M. 2000. Calcium carbonate modifications in the mineralized shell of the freshwater snail *Biomphalaria glabrata*. Chem. Eur. J. 6: 3679-3685.

Hild, S., Marti, O. and Ziegler, A., 2008. Spatial distribution of calcite and amorphous calcium carbonate in the cuticle of the terrestrial crustaceans *Porcellio scaber* and *Armadillidum vulgare*. J. Structural Biology 163: 100-108.

Ishitani ,T., and Yaguchi, T., 1996. Cross-sectional sample preparation by focused ion beam: A review of ion-sample interaction. Microsc. Res. Tech. 35: 320–333.

Jackson, D.J., C. McDougall, B. Woodcroft, P. Moase, R.A. Rose, M. Kube, R. Reinhardt, D.S. Rokhsar, C. Montagnani, C. Joubert, D. Piquemal, and B.M. Degnan, 2010. Parallel Evolution of Nacre Building Gene Sets in Molluscs. Molecular Biology and Evolution 27: 591-608.

Jacob, D.E., Soldati, A.L., Wirth, R., Huth, J., Wehrmeister, U. and Hofmeister, W., 2008. Nanostructure, chemical composition and mechanisms of bivalve shell growth. Geochim. Cosmochim. Acta 72: 5401-5415.

Kato, N.I., 2004. Reducing focused ion beam damage to transmission electron microscopy samples. J. Electron Microscopy, 53: 451-458.

Li, X., and Huang, Z., 2009. Unveiling the formation mechanism of pseudo-single crystal aragonite platelets in nacre. Physical Review Lett. 102: 075502.

Loges, N., Graf, K., Nasdala, L., and Tremel, W., 2006. Probing cooperative interactions of tailor-made nucleation surfaces and macromolecules: A bioinspired route to hollow micrometer-sized calcium carbonate particles. Langmuir 22: 3073-3080.

Lowenstam, H.A., and Weiner, S. 1989. On Biomineralization Oxford University Press.

Metzler, R.A., Abrecht, M., Olabisi, R.M., Ariosa, D., Johnson, C.J., Frazer, B.H., Coppersmith, S.N. and Gilbert, P.U.P.A., 2007. Architecture of columnar nacre, and implications for its formation mechanism. Physical Review Letters 98: 268102.

Mount, A.S., Wheeler, A.P., Paradkar, R.P. and Snider, D., 2004. Hemocyte-mediated shell mineralization in the Eastern Oyster. Science 304: 297-300.

Mutvei, H., 1977. The nacreous layer in Mytilus, Nucula, and Unio (Bivalvia). Calcif. Tissue Res. 24: 11-18.

Nassif, N., Pinna, N. Gehrke, N., Antonietti, M., Jäger, C. and Cölfen, H., 2005. Amorphous layer around aragonite platelets in nacre. Proceedings of the National Academy of Sciences of the United States of America 102: 12653-12655.

Neff, J.M., 1972. Ultrastructure of the outer epithelium of the mantle in the clam Mercenaria mercenaria in relation to calcification of the shell. Tissue Cell 4: 591-600.

Niederberger, M. and Cölfen, H., 2006. Oriented attachment and mesocrystals: Non-classical crystallization mechanisms based on nanoparticle assembly. Phys. Chem. Chem. Phys. 8: 3271-3287.

Nudelman, F., Chen, H.H., Goldberg, H.A., Weiner, S. and Addadi, L., 2007. Lessons from biomineralization: comparing the growth strategies of mollusc shell prismatic and nacreous layers in *Atrina rigida*. Faraday Discuss. 136: 9-25.

Petit, H., Davis, W.L. and Jones, R.G., 1980a. A scanning electron microscopy study of the inorganic and organic matrices comprising the mature shell of *Amblema*, a fresh-water mollusc. Tissue & Cell 12: 581-593.

Petit, H., Davis, W.L., Jones, R.G. and Hagler, H.K., 1980b. Morphological studies on the calcification process in the fresh-water mussel *Amblema*. Tissue & Cell 12: 13-28.

Pokroy, B., Fitch, A.N., Lee, P.L., Quintana, J.P., Caspi, E.N. and Zolotoyabko, E., 2006. Anisotropic lattice distortions in the mollusk-made aragonite: A widespread phenomenon. Journal of Structural Biology 153: 145-150.

Politi, Y., Metzler, R.A., Abrecht, M., Gilbert, B., Wilt, F.H. , Sagi, I., Addadi, L., Weiner, S. and Gilbert, P.U.P.A, 2008. Transformation mechanism of amorphous calcium carbonate into calcite in the sea urchin larval spicule. Proceedings of the National Academy of Sciences of the United States of America 105: 17362-17366.

Schäffer, T.E., C. Ionescu-Zanetti, R. Proksch, M. Fritz, D.A. Walters, N. Almqvist, C.M. Zaremba, A.M. Belcher, B.L. Smith, G.D. Stucky, D.E. Morse, and P.K. Hansma, 1997. Does Abalone nacre form by heteroepitaxial nucleation or by growth through mineral bridges? Chem. Mater. 9: 1731-1740.

Schöne, B.R., Dunca, E., Mutvei, H. and Norlund, U., 2004. A 217-year record of summer air temperature reconstructed from freshwater pearl mussels (*M. margaritifera*, Sweden). Quaternary Science Reviews 23: 1803-1816.

Soldati, A.L., Jacob, D.E., Schöne, B.R., Bianchi, M.M. and Hajduk, A., 2009. Seasonal periodicity of growth and composition in valves of *Diplodon chilensis patagonicus* (d'Orbigny, 1835). J. Molluscan Studies 75: 75-85.

515 Soldati, A.L., Jacob, D.E., Wehrmeister, U. and Hofmeister, W., 2008. Structural
516 characterization and chemical composition of aragonite and vaterite in freshwater
517 cultured pearls. Mineralogical Magazine, special issue on biominerals, 72 (2), 577-
518 590.
519 Strack, E., 2006. Pearls. 1. Edition ed. Rühle-Diebener Verlag, Stuttgart.
520 Tao, J.H., D.M. Zhou, Z.S. Zhang, X.R. Xu, and R.K. Tang, 2009. Magnesium-aspartate-
521 based crystallization switch inspired from shell moult of crustacean. Proceedings of
522 the National Academy of Sciences of the United States of America 106: 22096-
523 22101.
524 Ubukata, T., 1994. Architectural constraints on the morphogenesis of prismatic structure in
525 Bivalvia. Palaeontology 37: 241-261.
526 Watabe, N., Meenakshi, V.R., Blackwelder, P.L., Kurtz, E.M. and Dunkelberger, D.G., 1976.
527 Calcareous spherules in the gastropod *Pomacea paludosa*, p. 283-303, in: N. Watabe
528 and K. M. Wilbur, Eds.). The mechanisms of mineralization in the invertebrates and
529 plants, Univ. South Carolina Press, Columbia, S.C.
530 Wehrmeister, U., Soldati, A.L., Jacob, D.E., Häger, T. and Hofmeister, W., 2010: Raman
531 spectroscopy of synthetic, geological and biological vaterite – a Raman spectroscopic
532 study. J. Raman Spectroscopy 41: 193-201.
533 Wehrmeister, U., Soldati, A.L., Jacob, D.E., Loges, N., Häger, T. and Hofmeister, W., 2011.
534 Amorphous, nanocrystalline and crystalline calcium carbonates in biological
535 materials. J. Raman Spectroscopy, 42: doi:10.1002/jrs.2835.
536 Wehrmeister, U., Jacob, D.E., Soldati, A.L., Häger, T. and Hofmeister, W., 2007. Vaterite in
537 freshwater cultured pearls from China and Japan. The Journal of Gemmology 31:
538 399-416.
539 Weiner, S., 2008. Biomineralization: a structural perspective. J. Structural Biology 163: 229-
540 234.
541 Weiss, I.M., Tuross, N., Addadi, L. and Weiner, S., 2002. Mollusc larval shell formation:
542 Amorphous calcium carbonate is a precursor phase for aragonite. J. Exp. Zoology
543 293: 478-491.
544 White, W.B., 1974. The carbonate minerals, in Farmer, V.C. (ed.), The Infrared Spectra of
545 Minerals: Mineralogical Society of London Monograph 4:227-284.
546 Wirth, R., 2004. Focused Ion Beam (FIB): A novel technology for advanced application of
547 micro- and nanoanalysis in geosciences and applied mineralogy. Eur. J. Mineral. 16:
548 863-876.
549 Ziegler, A., 1994. Ultrastructure and electron spectroscopic diffraction analysis of the sternal
550 calcium deposits of *Porcellio scaber* Latr. (Isopoda, Crustacea). J. Structural Biology
551 112, 110-116.
552 Ziegler, A., 1997. Ultrastructural changes of the anterior and posterior sternal integument of
553 the terrestrial isopod *Porcellio scaber* Latr. (Crustacea) during the moult cycle. Tissue
554 Cell 29, 63-76.
555

556 **Figure Captions**

557 **Fig. 1:** Light microscope images of sectioned shells, showing the typical features of bivalve
558 shells in a *Diplodon chilensis patagonicus* shell (a): The periostracum covers the prism layer
559 which is followed by the nacre layer. Note the prominent growth lines extending into the
560 nacre layers, some of which are covered by intra-shell periostracum (arrow). (b) prisms
561 develop evenly or are terminated depending on geometric factors (*Hyriopsis cumingii* shell).
562 Initial prisms, protruding from the inner periostracum (c, here: *Hyriopsis cumingii*) show
563 prominent fine growth lines and have lower reflectance than prisms towards the ventral side
564 of the shell. These initial prisms at the periostracum interface (*Hyriopsis cumingii*) were
565 sampled by Focussed Ion Beam for TEM analysis (d). This method leaves a characteristic pit
566 in the material while the TEM-foil was extracted from the positions marked with "x" on both
567 sides of the pit. For a detailed description of the method see Wirth (2004).
568
569 **Fig. 2:** (A) Raman spectra of initial prisms in shells of the three bivalve genera (a: *Hyriopsis*
570 *cumingii*, b: *Diplodon chilensis patagonicus*) compared to ACC from *Porcellio scaber* (c) and
571 to crystalline biogenic aragonite from the nacre layer of *Diplodon chilensis patagonicus* (d).
572 The relative intensities are normalized to the highest peak in the spectrum, no baseline
573 correction was applied. The dashed line denotes the position of this band in ACC. 2(B)
574 shows the positions of the ν_1 band in the different spectra, highlighting the shifted position in
575 ACC compared to crystalline aragonite (spectrum d). Note the asymmetric ν_1 band in
576 spectrum c (*Porcellio scaber*) which is indicative of a mixture of crystalline and amorphous
577 $CaCO_3$.
578
579 **Fig. 3:** (a) FIB-foil, extracted from the periostracum-prism interface (Fig. 1d). Slight bending
580 of the foil occurred during milling which resulted in small gaps along the sides of the initial
581 prism in the middle of the foil (see also b) and lead to the development of slightly thicker
582 areas (darker grey in the middle of the foil). White frames shows the area enlarged in (b) and
583 (c), respectively. The black frame in the bright field TEM image (c) is enlarged in Fig. 4a.
584 Black arrows in (c) point to organic fibers between the $CaCO_3$ vesicles. The dark field TEM
585 image of the area (d) shows crystalline (white patches) and amorphous (without diffraction
586 contrast: white arrows) nanodomains. Calcium (e) and carbon (f) EELS maps demonstrate
587 that the depicted area consists predominantly of $CaCO_3$.
588
589 **Fig. 4:** A single vesicle (a, enlarged from Fig. 3c) was profiled along the white line by
590 HRTEM. While the rim (b) is nearly completely amorphous (see FFT analysis, e), except for a
591 ca. 5nm area circled in white, more nano-crystalline domains are observed toward the centre
592 of the vesicle (c, d). (e, f, g) are Fast Fourier Transform analyses of (b-d).

593 **Table 1:** Observed d-spacing values calculated from the HRTEM power spectra in Fig. 4 and
594 comparison to literature data for aragonite (JCPDS-ICDD 41-1475), vaterite (JCPDS-ICDD
595 33-268) and calcite (JCPDS-ICDD 5-586).

596

Observed			**Literature**					
Fig. 4e: Rim	Fig. 4f: Transition	Fig. 4g: Centre	Aragonite $(6_2)Pnma$		Vaterite $(194)P6_3/mnc$		Calcite $(167)R\text{-}3c$	
d_{hkl} [nm]	d_{hkl} [nm]	d_{hkl} [nm]	d_{hkl} [nm]	hkl	d_{hkl} [nm]	hkl	d_{hkl} [nm]	hkl
-	-	0.434	0.4212	110	0.4226	004	-	-
-	0.340	0.346	0.3397	111	0.3573	110	-	-
0.322	0.325	-	0.3274	021	0.3294	112	-	-
-	-	0.316	-	-	-	-	0.3040	104
0.226	0.230	-	0.2330	022	0.2282	205	0.2285	113
0.222	0.222	0.223	0.2190	211	0.2212	116	-	-
0.189	-	-	0.1882	041	0.1854	304	0.1875	116
-	0.181	0.181	0.1815	132	0.1820	118	-	-
-	-	0.169	0.1698	222	0.1646	224	-	-

597

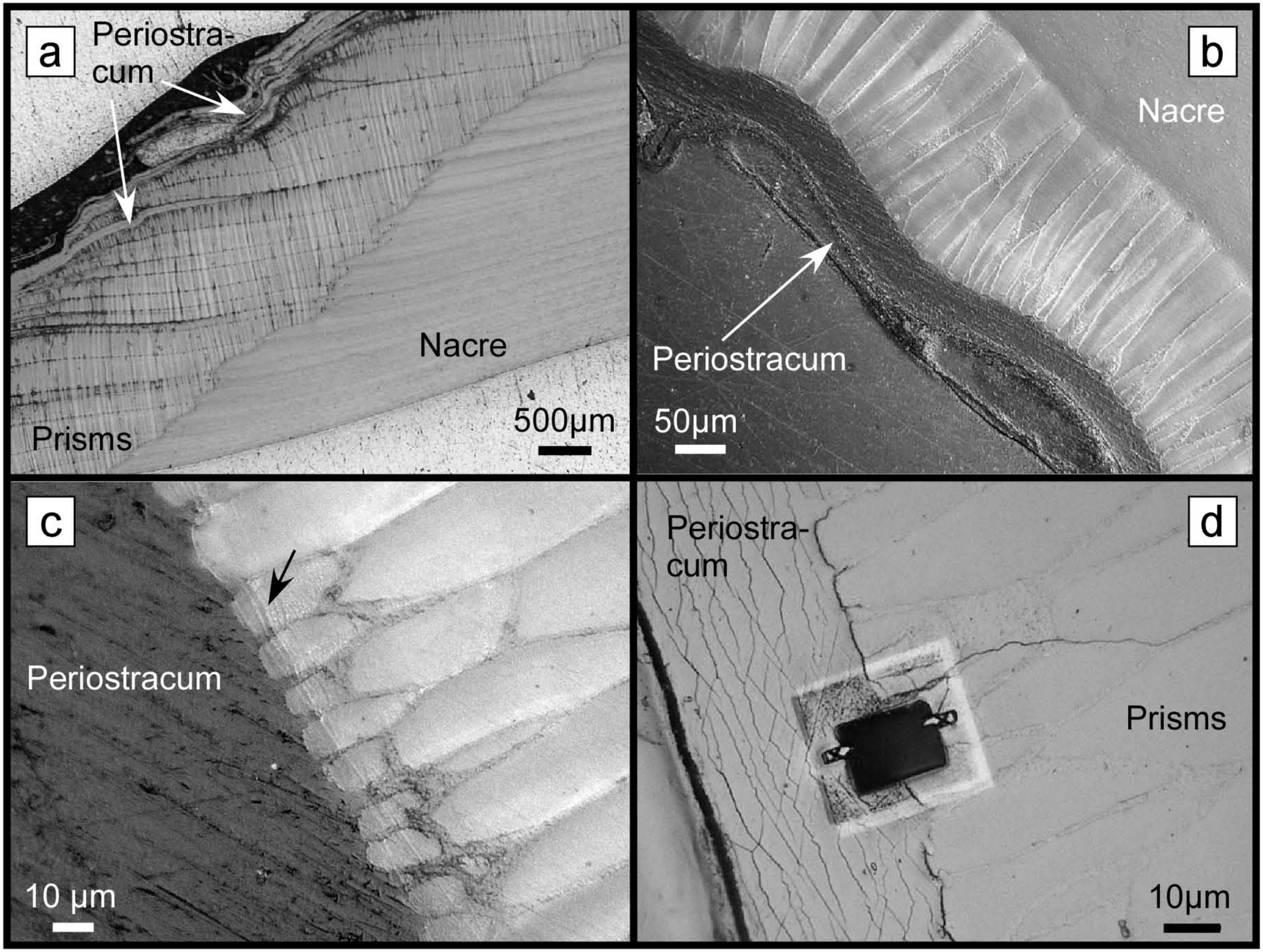

Fig. 1, Jacob, Wirth, Soldati, Wehrmeister, Schreiber

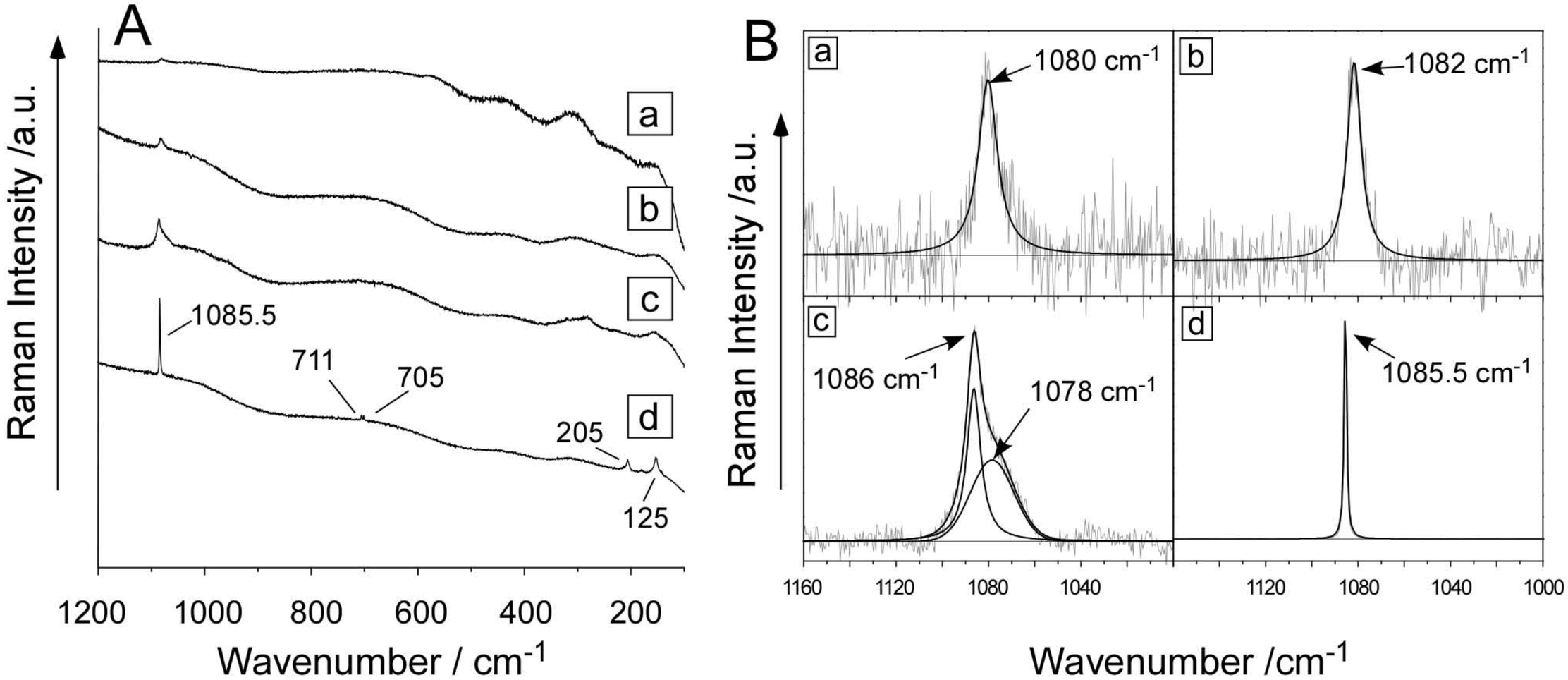

Fig. 2, Jacob, Wirth, Soldati, Wehrmeister, Schreiber

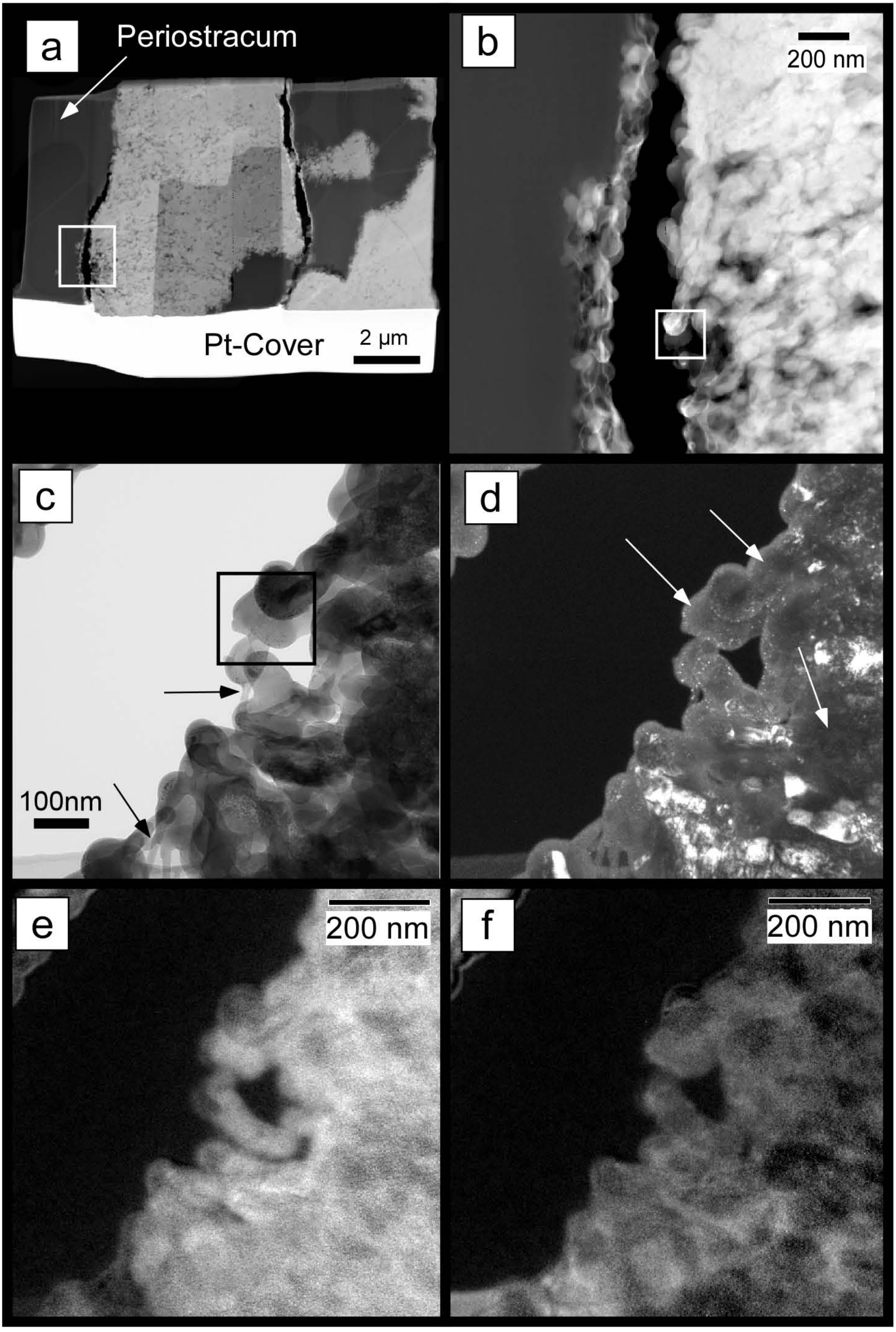

Fig. 3, Jacob, Wirth, Soldati, Wehrmeister, Schreiber

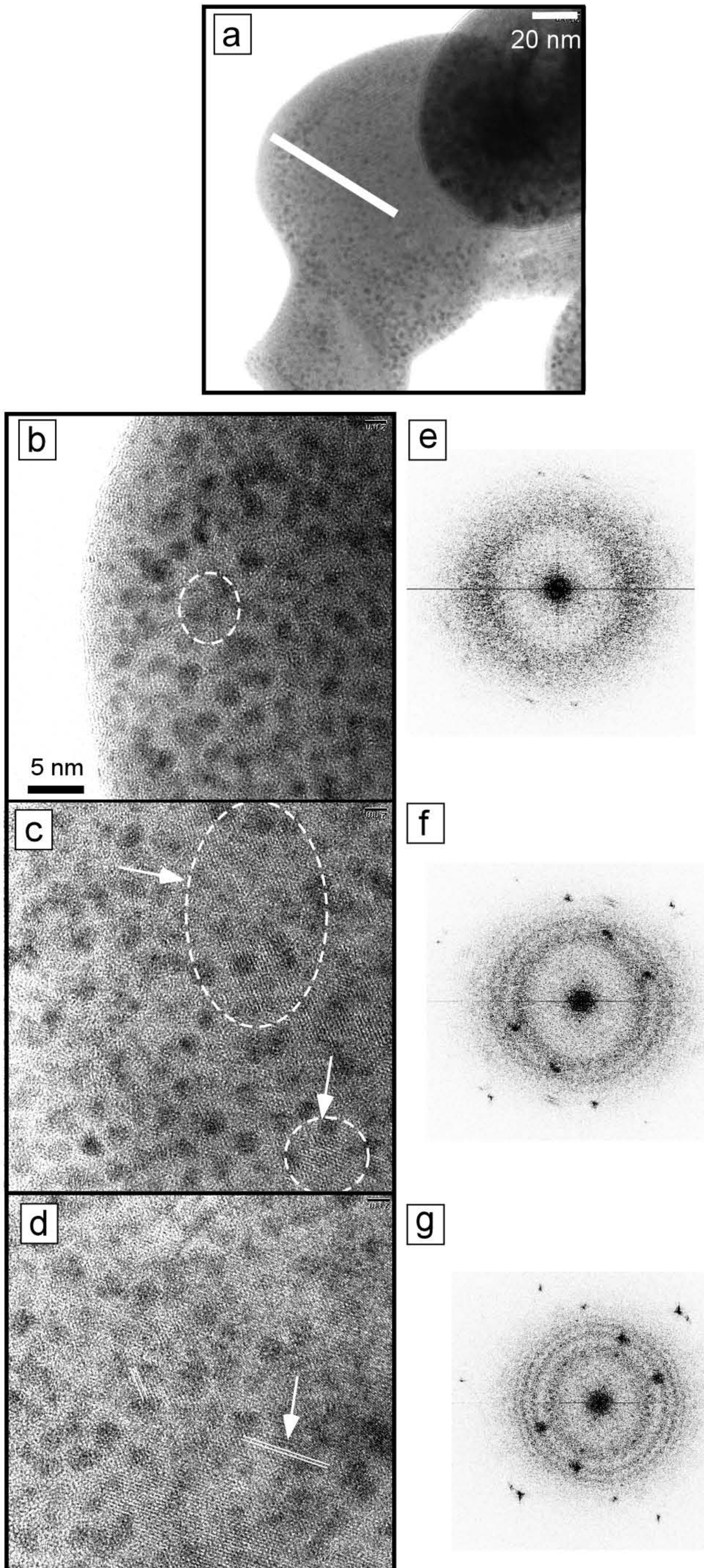

Fig. 4 Jacob, Wirth, Soldati, Wehrmeister, Schreiber